The Influence of Grain Shape and Size on the Relationship Between Porosity and Permeability in Sandstone

Ryan L. Payton[1,*], Domenico Chiarella[1] and Andrew Kingdon[2]

[1] Clastic Sedimentology Investigation (CSI), Royal Holloway, University of London, Department of Earth Sciences, Egham, Surrey, United Kingdom

[2] British Geological Survey, Keyworth, Nottingham, United Kingdom

[*] Corresponding author: ryan.payton.2015@live.rhul.ac.uk

Twitter Handles:

RLP: @RyanLPayton

DC: @nocode_dc

AK: @AndyGeology

CSI: @CSI_RHUL

RHUL Earth Sciences: @RHULEarthSci

ABSTRACT

An accurate and reliable description of the relationship between porosity and permeability in geological materials is valuable in understanding subsurface fluid movement. This is of great importance for studies of reservoir characterisation, useful for energy exploitation, carbon capture, use and storage (CCUS) and groundwater contamination and remediation. Whilst the relationship between pore characteristics and porosity and permeability are well examined, there is scope for further investigation into the influence of grain characteristics on porosity and permeability due to the inherent relationship between grains and related pores. In this work we use digital image analysis (DIA) of reconstructed 3D X-ray micro computed tomographic (μCT) images to measure porosity, permeability and segment individual grains enabling the measurement of grain shape (sphericity) and size (Feret diameter). We compare two marker-based watershed workflows to grain boundary segmentation before applying the most reliable one to our images. We found there to be a positive relationship between grain sphericity and porosity according to $\phi = 1.22\phi_s - 0.42$ whereas no such relationship exists with grain size. We applied our grain shape and size measurements to calculate a Kozeny-Carman (K-C) porosity-permeability fit which was found to be unsatisfactory, possibly due to significant deviation from the K-C assumption that grains are spherical. Therefore, we show that a simpler fit of the form $K = 10^{5.54}\,\phi^{3.7}$, excluding any influence of grain characteristics, is most

suitable for the studied materials and that grain shape and size is not influential on the porosity-permeability relationship in a K-C paradigm.

INTRODUCTION

The relationship between porosity and permeability is very significant for reservoir characterisation studies applied to energy exploitation, carbon storage and aquifer contamination and remediation. Constraining the relationship between these two important reservoir parameters is beneficial as measurement of porosity alone can then be used to predict permeability, which is typically expensive and time consuming to measure both physically in a lab and computationally using digital image analysis (DIA). Furthermore, permeability can only be measured directly in the lab on small scale samples or in the field at the macro scale using pump tests, producing two results which often do not closely agree. Therefore, identification of a reliable and accurate relationship between porosity and permeability using computed tomography (CT) imaging could have far-reaching implications for reconciling this issue.

Modelling a Porosity-Permeability Relationship

The Kozeny-Carman (K-C) relationship, proposed by Kozeny (1927) and later modified by Carman (1937), is a simple yet broadly effective and widely used (Mavko and Nur 1997; de Lima and Sri Niwas 2000; Urumovic and Urumovic Sr.

2014; Berg 2014; Hommel et al. 2018) technique of relating porosity to permeability. Bear (1972) suggested a modification to the K-C equation which allows grain diameter to be employed as a component which influences the permeability. Additionally, Hommel et al. (2018) show that an additional grain sphericity term may also be used. Whilst a K-C-based approach is successful in many instances, its accuracy may be questioned when applied to materials which possess a significant proportion of grains which deviate substantially from being spherical. The limitation of a K-C approach is that grains are considered spherical and packed in a regular arrangement; allowing pores to be considered as capillary bundles. The inherent relationship between the pore structure and the grains which create the pore space indicates that a detailed investigation of grain characteristics is of utmost importance in understanding the porosity-permeability relationship.

In this work we aim to investigate whether the inclusion of grain sphericity and 3D Feret diameter (referred to herein as grain size) in a K-C paradigm facilitates a better quality fit to the relationship between porosity and permeability. We compare our modified K-C approach to a simpler fit using porosity and permeability measurements alone, excluding any influence of grain shape or size. To do so, the individual relationships between porosity and permeability and grain sphericity and size are investigated and considered in light of the concept of grain anisotropy, as introduced by Nabawy (2014).

A Methodology for Making Digital 3D Grain Measurements

Whilst grain size and shape measurement has traditionally been done manually using callipers and sieve analysis (W. D. Keller 1945; Schäfer and Teyssen 1987; Wang et al. 2013; Suhr et al. 2018) we have used digital image analysis (DIA) to segment individual grains in 3D using reconstructed X-ray micro computed tomographic (μCT) image stacks of each sample. μCT imaging has been used in a wide variety of fields related to geosciences since its rise in popularity as a non-destructive and high resolution image acquisition technique (Blunt et al. 2013; Bultreys et al. 2015; Thomson et al. 2018, 2020b; Payton et al. 2021). When paired with DIA, large amounts of quantitative and visually useful data may be obtained. Unlike when using optical imaging, X-ray imaging is dependent primarily on phase density therefore, grain boundaries are difficult to identify, particularly in a tightly packed sandstone.

In this work we discuss and investigate grain segmentation using two relatively simple marker-based watershed workflows. Watershed algorithms, established by Beucher & Meyer (2018), split a phase up into individual components by treating the image as a topographic surface, identifying topographic lows and assigning a seed point to each. Flooding from each seed point allows digital watersheds to be identified and are used to define the boundaries between individual features (Sun et al. 2019). The challenge arises from making correct identification of marker points so as not to have multiple grains sharing one marker (undersegmentation) or the opposite where multiple markers are assigned to a single grain (oversegmentation). Techniques such as the bring up (Kong and Fonseca 2018; Leonti et al. 2020) and bring down (Shi and Yan 2015; Sun et al. 2019) methods have been developed to try and tackle this issue but can often be computationally demanding and may still produce inaccuracies.

Segmentation of the solid phase alone allows identification of individual grains which can then be measured digitally in 3D. Segmentation is arguably the most important and usually most difficult process in DIA (Campbell et al. 2018) given that poor segmentation will directly result in poor and likely misleading results. It is notoriously difficult to segment features within a given phase which are touching, consequently many techniques have been developed to tackle this challenge, often providing unique solutions to a given sample set or type of sample (shelly, angular, rounded, etc…) (Campbell et al. 2018; Kong and Fonseca 2018; Furat et al. 2019; Leonti et al. 2020) as there is not a one size fits all solution (Campbell et al. 2018).

We assess two segmentation workflows and use the most effective to analyse a collection of 22 sandstone samples from three different geological formations (i.e., Wilmslow Sandstone Formation, Sellafield, UK; Brae Formation Sandstone, Miller Field, North Sea, UK; Minard Formation Sandstone, Porcupine

Basin, North Atlantic Ocean). Finally, we use the grain measurements alongside digital measurements of porosity and permeability to investigate the quality of a K-C-based fit to the porosity-permeability relationship using grain shape and size inputs.

METHODS

A variety of sandstone samples have been selected from several different reservoir units which host significant levels of porosity. Samples from the Wilmslow Sandstone Formation (Sellafield, UK; Payton et al. 2021), Brae Formation Sandstone (North Sea, UK; Thomson et al. 2020b) and the Porcupine Basin (North Atlantic Ocean) were acquired and imaged at the London Natural History Museum Imaging and Analysis Centre. Table 1 summarises the materials used in this work and specifies the associated literature detailing initial sample imaging where relevant. We chose to exclude samples which exhibited no connected porosity and therefore no permeability for the purpose of this study.

The material pertaining to the Porcupine Basin was collected and prepared using the same technique outlined by Thomson et al. (2020b) and Payton et al. (2021). From each sample a mini plug measuring 5 mm in diameter and 10 mm in length was cut and imaged using X-ray micro computed tomography (μCT), detailed by Payton et al. (2021). For further information about the voxel size and subsampled volume of each sample we refer the reader to the Supplementary Information.

Image Processing

The acquired µCT image stacks of each sample underwent pre-processing using the commercial software package PerGeos (v1.7.0). From each image stack a sub-volume was extracted to remove external voxels and any image slices which contained significant beam hardening artefacts. In order to aid the segmentation process we employed a non-local means filter which enhances the contrast between greyscale phases and removes speckled noise throughout the images (Buades et al. 2008, 2010).

Porosity and Permeability

We followed the method detailed by Payton et al. (2021) to measure porosity and permeability - a brief outline is described here. We made use of the well-known automatic binary segmentation algorithm designed by Otsu (1979) to separate and label the solid grain phase and pore space. In some cases, it was necessary to constrain the greyscale range over which the algorithm was allowed to operate on where exceedingly bright phases were present which meant darker grains and darker pore space were not automatically separated.

The volume fraction of the segmented pore space can be measured which equates to the total sample porosity. We then applied the 'axis connectivity' tool along each axis in turn to determine the proportion of porosity which is entirely connected between all faces of the sample. We took this value to represent the connected porosity.

Finally, we employed the 'absolute permeability simulation' tool to run a finite difference numerical simulation, solving the Stokes flow equations:

$$\nabla \boldsymbol{u} = 0 \tag{1}$$

$$- \nabla P + \mu \nabla^2 \boldsymbol{u} = 0 \tag{2}$$

where $\boldsymbol{u}$ is velocity, P is pressure, μ is fluid viscosity equal to 1×10^{-3} Pa s for water. We used an error tolerance of 10^{-6} for the convergence of the L_2 norm of the residuals as recommended by Thomson et al. (2019) whilst the boundary conditions used are discussed in detail by Thomson et al. (2018). The solution is a velocity field which allows for a permeability value to be determined through application of Darcy's Law. Further details on this technique can be found in Thomson et al. (2020b) and Payton et al. (2021).

Pore Geometry

In order to characterise the individual pores which make up the pore structure we employed a pore network model (PNM). PNMs are simplified representations of complex pore geometries using balls to represent pores and sticks to represent throats. We created PNMs of the connected porosity following the methodology detailed in Payton et al. (2021) and references therein. Each PNM may be interrogated to provide information about each pore including radius and coordination number, and each throat including radius and length.

Grain Segmentation

Segmentation of individual features in µCT images has traditionally been performed using the marker-based watershed approach detailed by Beucher & Meyer (2018). This technique has been widely used in a variety of fields (Barraud 2006; Cristoforetti et al. 2008; Veta et al. 2011; Huang et al. 2018; Xue et al. 2021) to identify and split individual features in digital images. The general steps in using a watershed algorithm are shown in Figure 1 (for a more detailed description of how a watershed algorithm operates we refer the reader to Kong & Fonseca (2018) and Sun et al. (2019)). We chose to follow the workflow of watershed segmentation of grains described by Fei & Narsilio (2020) which is shown to be

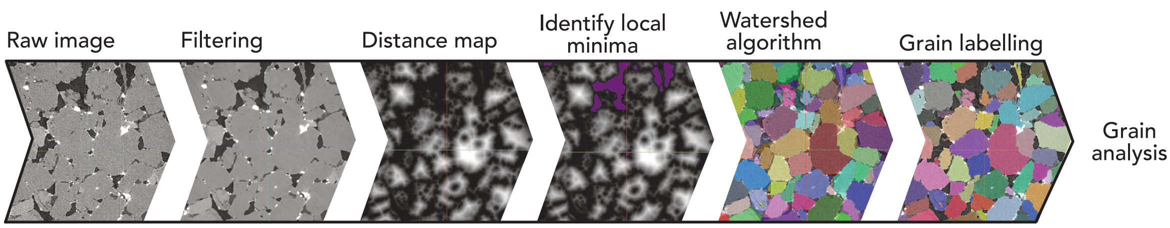

successful in separating grains in a variety of different sand samples which bare some resemblance to the materials investigated here.

Figure 1

The method described by Fei & Narsilio (2020) uses the software package Fiji (Schindelin et al. 2012) to carry out cropping and filtering. A non-local means filter is used in combination with a median filter prior to using the MorphoLibJ plug-in for Fiji (Legland et al. 2016) which encompasses generation of a distance map and identification of seed points for watershed flooding as described in Figure 1.

Grain Measurements

Once the watershed algorithm has run, the individual grains are labelled before the Feret diameter and sphericity of each grain is measured using the 3D ImageJ Suite plug-in (Ollion et al. 2013). When extracting 3D grains from µCT images, which are voxelised, the edges exhibit a saw-tooth pattern (Fig. 2). This can lead to overestimation of surface area and consequently underestimation of sphericity, as detailed by (Fei et al. 2019). Therefore, we acknowledge that our sphericity measurements are conservative but as the saw-tooth pattern effect is present for all grains measured, the results we present are still directly comparable between each other.

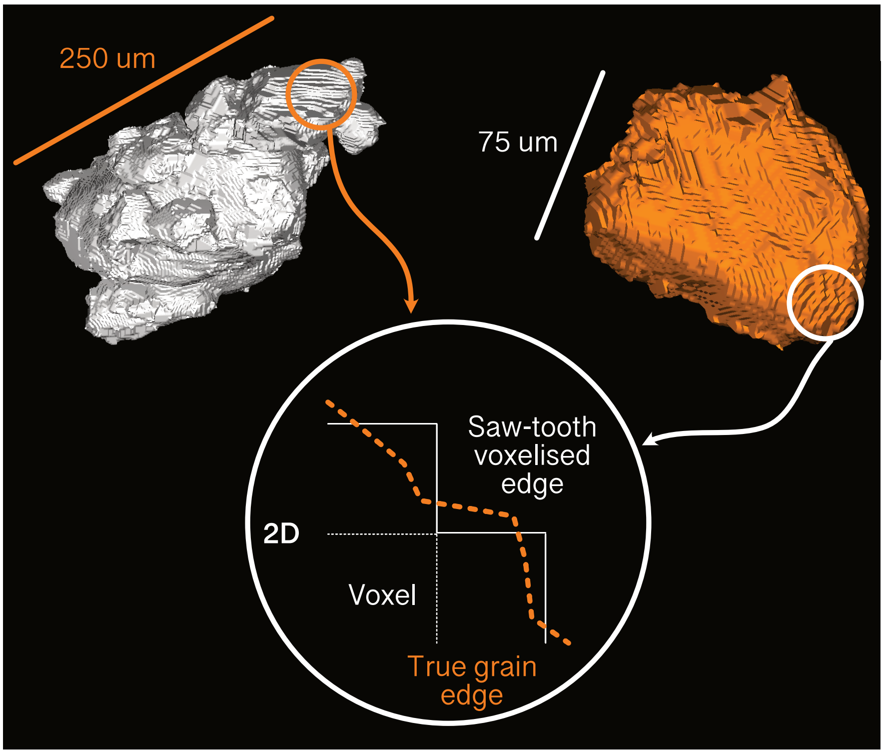

Figure 2

Whilst smoothing algorithms can be applied to reduce this effect, determining appropriate parameters for such algorithms becomes heavily subjective and can cause undesirable deformation of the individual grains such as volume loss. Moreover, using the same degree of smoothing on a very small and a very large grain will have different impacts on the resulting shape. Consequently, we chose to omit the use of any smoothing tools prior to our measurements being made.

The automated nature of the MorphoLibJ and 3D Suite plug-ins enables this analysis to be carried out simply as well as rapidly with low computational cost. Sphericity is measured between 0 and 1 where 1 represents a perfect sphere. We used Feret diameter as the representative grain size for all statistical analyses in this work. Some of the grain size analyses performed use phi (ϕ) units, calculated from grain size values in millimetres according to:

$$\phi = -\log_2 D \tag{3}$$

where D is the grain diameter. We calculated the graphic mean grain size (M_Z) after Folk (1980) according to the following formula:

$$M_Z = \frac{(\phi 16 + \phi 50 + \phi 84)}{3}, \tag{4}$$

where $\phi 84$ represents the ϕ value at the 84th percentile. We calculated the 'inclusive graphic standard deviation' introduced by Folk (1980) to determine the sorting (ϕ_1) of our samples using the following formula:

$$\phi_1 = \frac{\phi 84 - \phi 16}{4} + \frac{\phi 95 - \phi 5}{6.6}. \tag{5}$$

We then classified the sorting of our samples following the accompanying scheme defined by Folk (1980) where a smaller ϕ_1 value is representative of better sorting.

RESULTS

Application of the Proposed Methodology

Each study sample was analysed in terms of grain characteristics and the results are reported in Table 2. The accompanying porosity and permeability results are reported in Table 3, measured in this article and by Thomson et al. (2020b) and Payton et al. (2021). Figure 3 shows the relationships among mean grain size, mean grain sphericity, porosity, and permeability. No clear relationship between grain size and sample porosity or permeability is observed (Figs. 3a and

3c). Despite this, we see a much clearer positive correlation between the grain sphericity and porosity and permeability (Figs. 3b and 3d). This suggests that the shape or anisotropy of the grains has a direct influence on the pore structure whereas the size of the grains does not. Figure 3d highlights a collection of seven

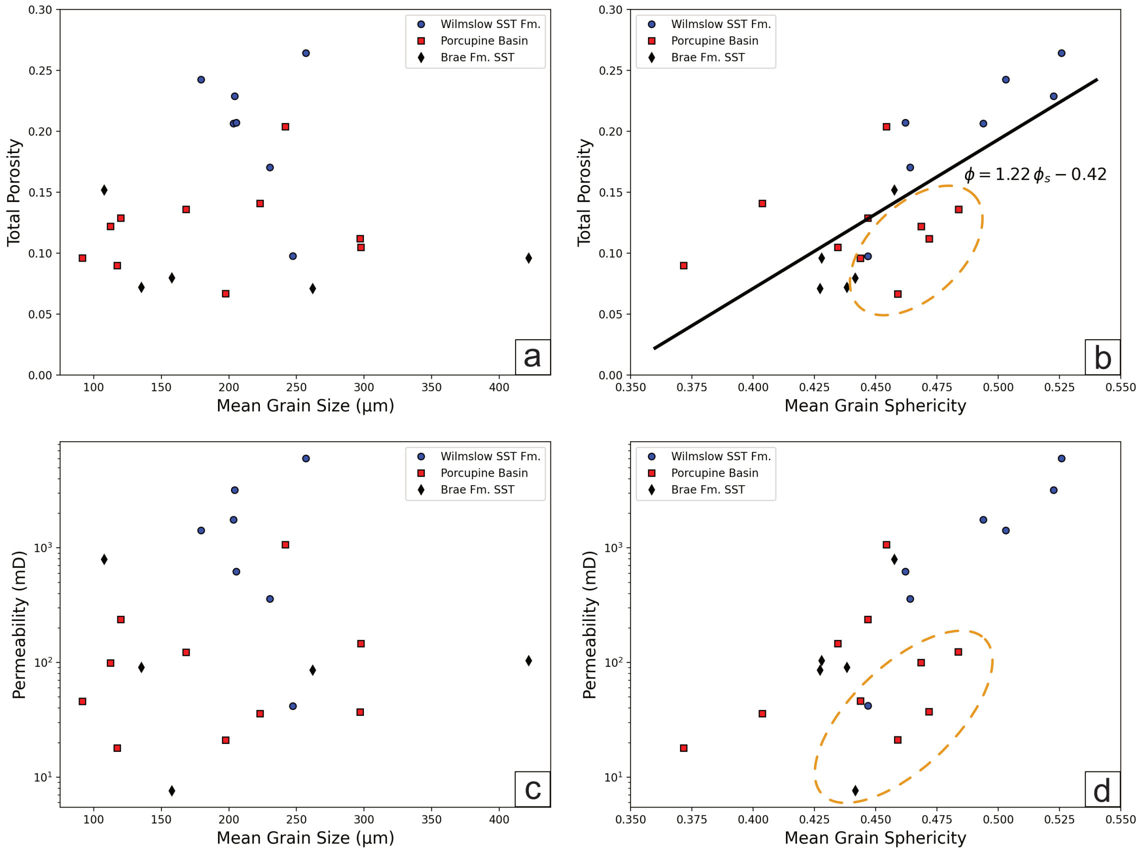

outliers showing the same relationship but offset from the dominant trend between mean grain sphericity and permeability. The same collection of data points is highlighted in Figure 3b, plotting mean grain sphericity against total porosity, where they are not obviously misaligned with the rest of the data points. This indicates that these apparent outliers, in the case of permeability, result from a characteristic of the sample which is independent of porosity but not permeability.

262 **Figure 3**

263 As the intergranular porosity is fundamentally governed by the grains
264 themselves, we investigated the relationship between the pore structure and
265 grain sphericity. Figure 4 shows a generally positive relationship between grain
266 sphericity and the connected pore diameter except for four apparent outliers
267 across all three sample suites. Of these four outliers, two belong to the group of
268 seven identified in Figure 3d and two do not. However, the cause for the
269 occurrence of these four outliers is unclear and it seems that there is no
270 correlation between these four outliers and other measured factors such as
271 sorting and grain size.

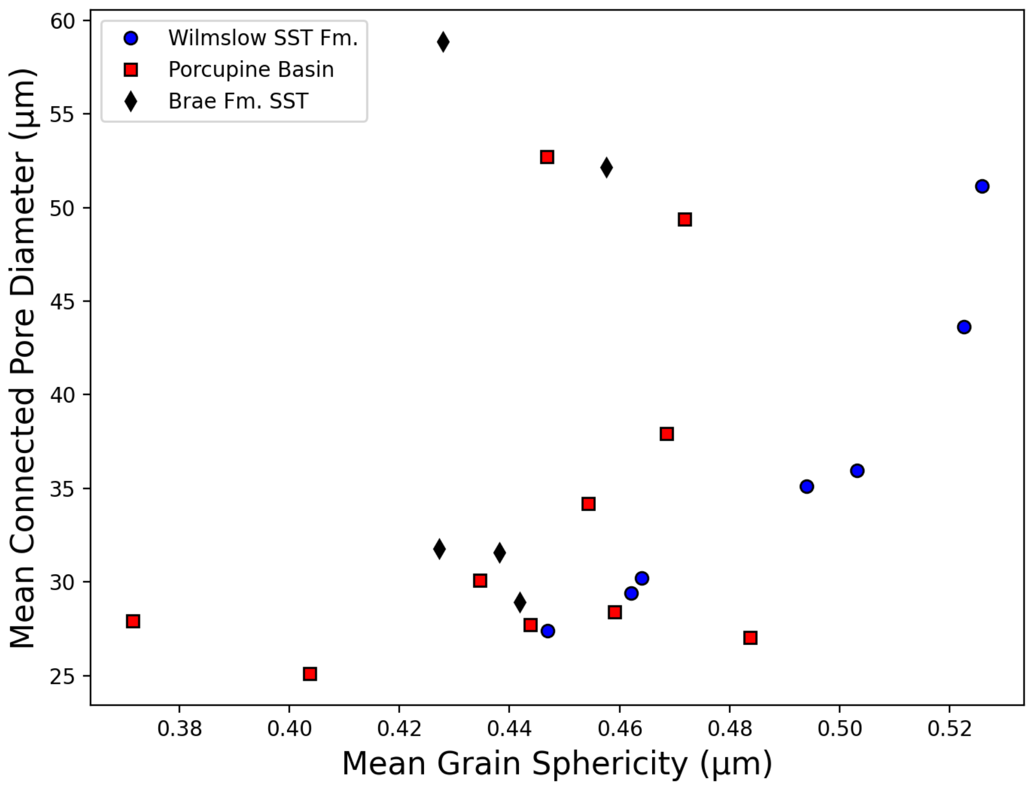

272 **Figure 4**

Impact of Grain Shape on the Porosity-Permeability Relationship

Our results show that the shape of the grains in a sample has an impact on the porosity and permeability. Therefore, it is reasonable to assume that the porosity-permeability relationship could be better constrained through incorporating the grain shape into the fit equation. Accordingly, we employed a modified Kozeny-Carman equation discussed by Hommel et al. (2018),

$$K = K_0 \frac{\phi_s^r \, \phi^n \, D_p^m}{180 \, (1-\phi)^2}, \tag{6}$$

which incorporates the grain sphericity, ϕ_s and size, D_p alongside porosity, ϕ and a permeability constant, K_0 to calculate a porosity-permeability fit. We imposed a variety of constraints on the fit with regards to the three constant exponents: n, m and r, applicable to porosity, grain size and grain sphericity respectively (Fig. 5), to determine the best fit with the lowest root mean square error (RMSE).

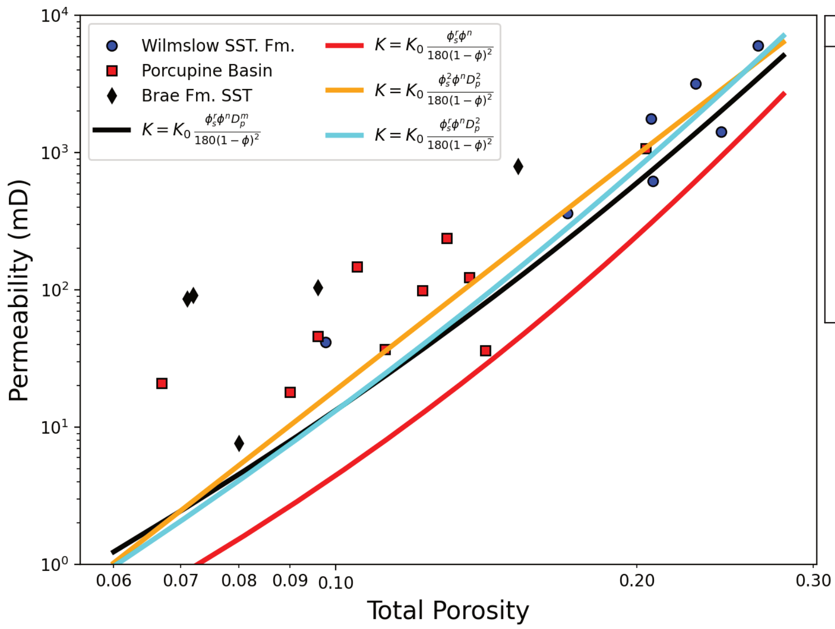

Fit Line	Characteristics
Black	Includes all terms, all exponents are unconstrained
Red	Excludes the grain size term, all exponents are unconstrained
Orange	Includes all terms, only the porosity exponent is unconstrained
Blue	Includes all terms, both the porosity and grain sphericity exponents are unconstrained

Figure 5

The best of the four fits based on the RMSE (Fig. 5) is the case where each exponent can vary and is not constrained in any way, shown by the black fit line. The red fit line, which omits the grain size term, produces the poorest quality fit even though we identified grain size to have no relationship with porosity or permeability (see Figs. 3a and 3c). The remaining two fit lines in cyan and orange offer fits with RMSE values just larger and therefore less successful than the black fit. The cyan and orange fits offer varying constraint on the exponents of grain size alone and grain size alongside grain sphericity respectively but importantly, both include the grain size term. Inclusion of this term, whether its exponent may vary or not, clearly allows the given fit to be of a greater quality than omitting it all together.

It is apparent that even the best fit achieved, shown by the black line in Figure 5, does not fit all data points effectively, especially below a total porosity of ca. 15%. Consequently, we show an additional, simpler fit which does not consider any grain characteristics in Figure 6 (green line) alongside the best fit identified in Figure 5. Our results show that the simpler fit which considers porosity and permeability alone is more effective, exhibiting a lower RMSE of 1.39 as opposed to 1.67 in the case of the fit incorporating the grain characteristics.

Figure 6

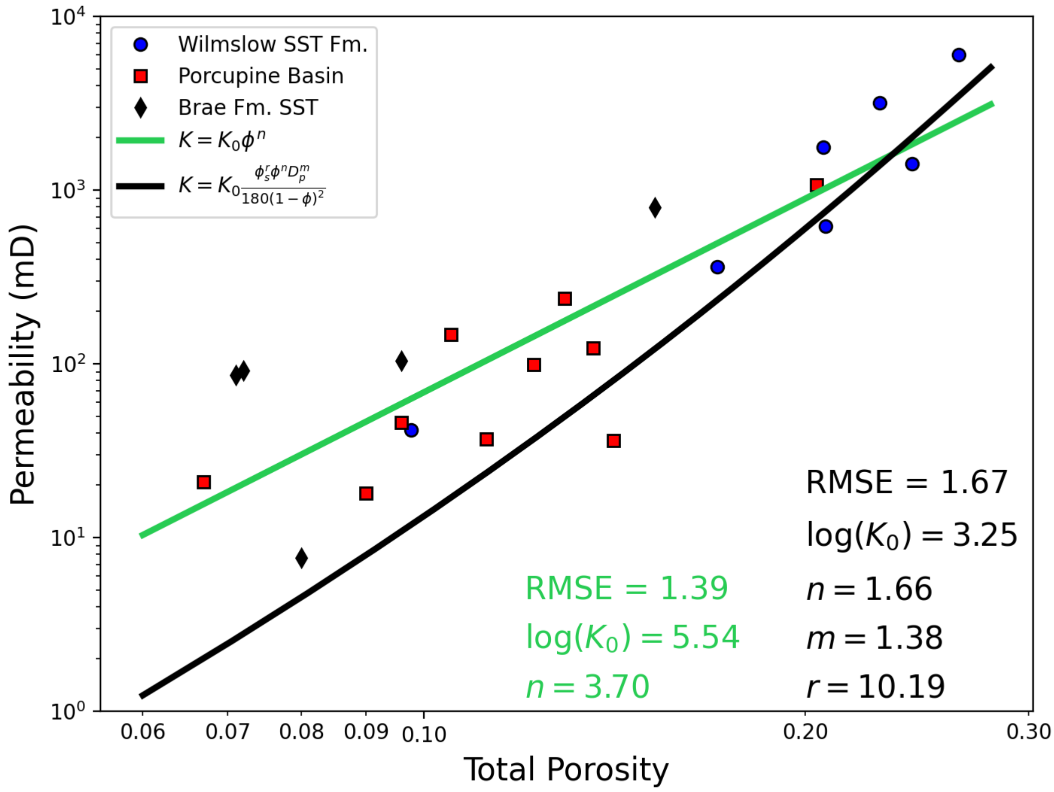

DISCUSSION

Grain Boundary Watershed Segmentation

Whilst the approach that we take to segment individual grains (Fei and Narsilio 2020) is relatively straightforward, we acknowledge that there are a number of other algorithms which aim to improve the accuracy of the traditional watershed algorithm. In particular, oversegmentation is an issue, particularly when segmenting features of a wide range of sizes and shapes where multiple markers are placed within one feature (Kong and Fonseca 2018; Sun et al. 2019; Leonti et al. 2020). Modified watershed approaches have been developed using the bring down method (Shi and Yan 2015) and the bring up method (Kong and Fonseca 2018; Leonti et al. 2020) to accurately label features and their boundaries. Due to the high accuracy of results reported by Fei & Narsilio (2020), the ease of implementation and minimal computational cost we chose to use the traditional watershed technique with a non-local means and median filter in line with the methodology described by the authors.

The technique used here is very similar to that applied by Thomson, et al. (2020a). Thomson, et al. (2020a) implement a traditional watershed algorithm but only use a non-local means filter without a median filter. The non-local means filter performs the bulk of the denoising in the images very effectively, but this type of filter is not optimal for retaining or improving feature boundaries. In contrast, the median filter is very effective for this purpose, enhancing the clarity of feature boundaries whilst smoothing any remaining noise in the images. We show the similarities and differences in the results of watershed segmentation using the two approaches in Figure 7.

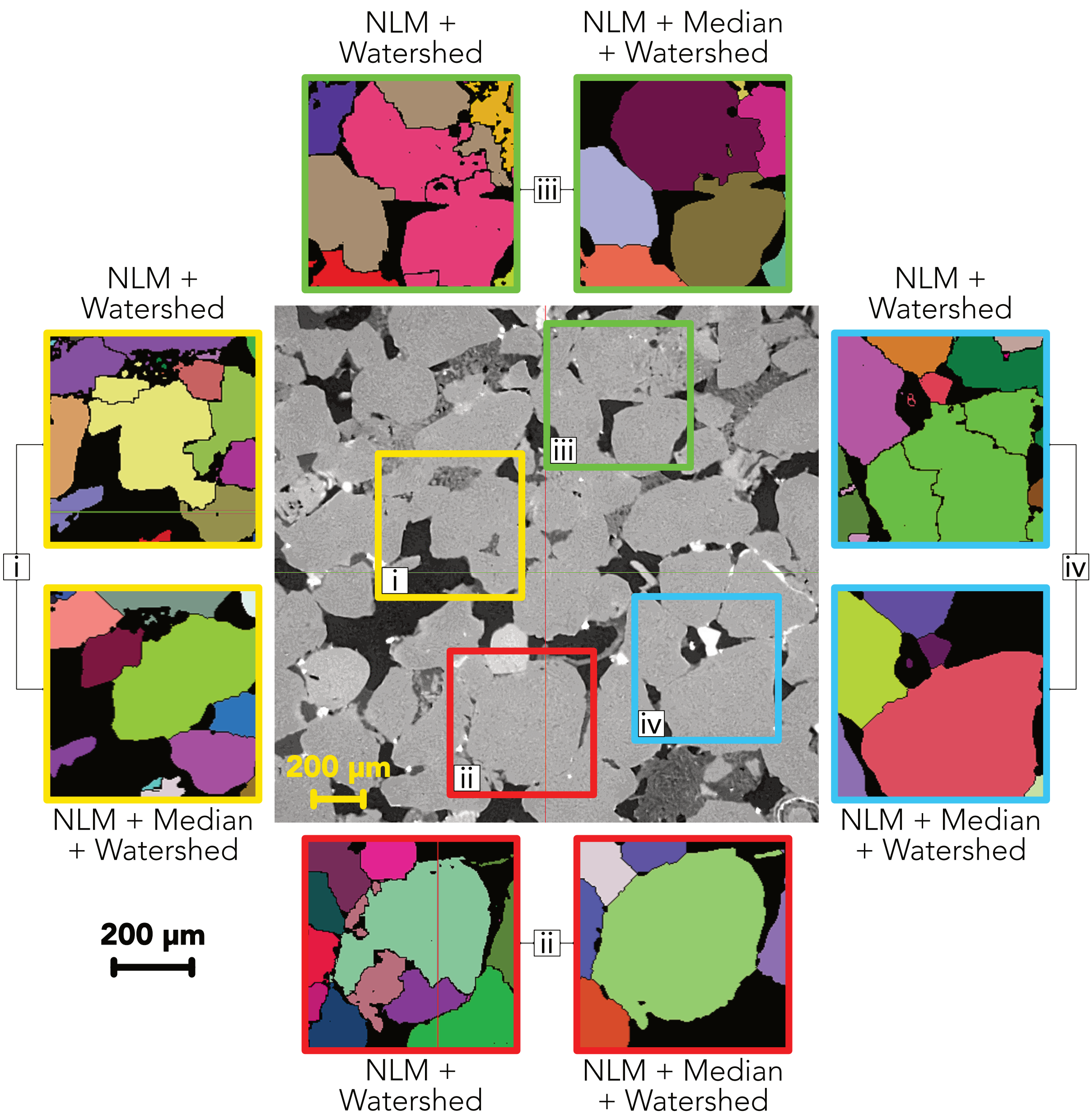

329 **Figure 7**

330 Our results show that the approach used by Thomson, et al. (2020a) results
331 in some oversegmentation of grains when comparing the watershed result to the
332 greyscale CT image. In contrast the approach used in this study does not show
333 severe oversegmentation of the same grains, owing to the boundary
334 enhancement provided by the median filter. Furthermore, by using the 3D Suite
335 plug-in for Fiji, grains which are touching the boundaries of the study volume can

be excluded from measurement to ensure only grains which are complete and truly representative are included. This was not included in the method used by Thomson, et al. (2020a) and therefore partial grains may have significantly influenced the mean grain measurements made.

Finally, Thomson, et al. (2020a) acknowledge in their work that the separated grains in their work displayed an unexpected group of grains with Feret diameters of < 63 μm, smaller than the classification of sand grains following the scheme proposed by Wentworth (1922). Employing the additional median filter largely removed the occurrence of these small, unexpected grains. Therefore, we suggest that the combination of a median filter with a non-local means filter is effective in reducing over segmentation and identification of small, unexpected features.

The Influence of Grain Characteristics

Grain Size and Shape.--- The observed lack of relationships between mean grain size and both porosity and permeability (Figs. 3a and 3c) strongly suggests that grain size within this suite of samples is not influential on the porosity-permeability relationship of the respective pore structures. Nabawy (2014) presents a similar conclusion when examining the influence of grain size on porosity and permeability in a series of idealised grain packs as well as in high porosity sandstone samples. All but two of our samples are classified as very well-well- or moderately-sorted (Folk 1980). Therefore, we suggest that future work should focus on the relationship between grain size and porosity and permeability in a variety of sandstones of different grain maturity, shape and facies to identify any factors which may influence whether grain size presents a relationship with porosity or permeability.

In contrast, we show evidence that mean grain sphericity has a direct positive impact on both porosity and permeability (Figs. 3b and 3d). Nabawy (2014) identifies a similar relationship with the elongation (grain length/grain diameter) of grains within their sample suite where less elongate grains contribute to greater porosity and permeabilities. Nabawy (2014) uses elongation as a measure of grain anisotropy where a more elongate grain indicates a greater degree of anisotropy. We can apply the same approach to grain sphericity, where a less spherical grain indicates a greater degree of anisotropy. Following this paradigm, we see that our results agree with those of Nabawy (2014), a greater degree of anisotropy of the grains results in a reduction in both porosity and permeability.

We calculated a simple linear fit for the relationship between mean grain sphericity and total porosity which is given by $\phi = 1.22\,\phi_s - 0.42$. Nabawy (2014) proposes a relationship between elongation, E and porosity using their sample suite where $\phi = 45.73\,E^{-1} + 9.19$. This provides two parameters by which a porosity estimation may be made based upon two different measures of grain anisotropy. Whilst Nabawy (2014) achieves an elongation fit exhibiting a correlation coefficient of 0.92 we find our sphericity fit to have a correlation coefficient of 0.65. We consider three separate sample suites from different sedimentary facies, whilst Nabawy (2014) focusses on a single sample suite, which makes the relationship between anisotropy and porosity less clear. Consequently, we suggest that different depositional environments may have a more significant effect upon the characteristics which influence the relationship between grain anisotropy and porosity, as opposed to there being one consistent relationship being applicable across a wide variety of sandstones. Further research is required to quantify the scale of this influence

We also investigated the control which the anisotropy of grains has on the geometry of the pores themselves, finding that there is generally a positive relationship between grain sphericity and pore diameter (Fig. 4). Our results agree with the relationship identified between porosity and grain anisotropy, measured through elongation (Nabawy 2014). This indicates that these two measures of grain anisotropy exhibit similar controls on porosity which reflects directly in the geometry of the pore structures.

A suggested limitation of the relationship reported by Nabawy (2014) is that it may depend on grain elongation occurring systematically along one axis which is common throughout the sampled material. Such imbrication of grains according to their elongation axes may result due to the flow of depositional currents and load pressure. Where such an alignment is not clearly present, for example under depositional conditions where turbulent flow dominates, these results imply that the detrimental impact on permeability would be far more pronounced than any influence on the relationship with porosity. This conclusion requires further testing using samples from varied depositional environments to eliminate the effects of sorting and stratification.

We observe an apparent group of seven outliers when examining the relationship between grain sphericity and permeability (Fig. 3d) which fall below the dominant trend. The fact that this group of outliers are not apparent when comparing sphericity with porosity (Fig. 3b) strongly suggests that their rogue placement is due to a factor which inhibits fluid flow but does not change the absolute porosity measurement. This may point towards a lack of preferential orientation with regards to grain anisotropy within these particular samples.

Further investigation of the seven outliers found that there was no apparent common characteristic amongst the outliers which could differentiate them from the remaining samples. We investigated whether there was a relationship between these outliers and their sample depth, sorting, porosity or permeability which might explain their occurrence. None of these characteristics helped to explain the presence of the seven outliers. Furthermore, a qualitative assessment of the μCT images found nothing of significance which might allow for the differentiation of this sample group such as presence of cement or other precipitates which were not present in the main group of samples.

It might be expected that a lack of grain orientation would manifest throughout a given geological unit, leading to surprise that the outlier group contains at least one sample from each of the three studied formations. We suggest that the resulting texture may be controlled by a different depositional process. Alternatively, the scale of the sample upon which measurements were made could be considered not suitably representative for the scale of the processes which cause variation in grain imbrication and alignment with regards to anisotropy. Therefore, we suggest that future work should focus on identifying a suitable representative elementary volume over which measures of grain anisotropy, such as elongation and sphericity, can be representatively measured. Equally, identification and implementation of a technique to measure and quantify alignment or imbrication of grains in 3D at the pore scale would be beneficial in providing greater context for relationships between porosity and permeability with measures of grain anisotropy.

Grain Influence on the Porosity-Permeability Relationship.--- Despite the positive relationship identified between mean grain sphericity and porosity and permeability (Figs. 3b and d) we have found that the influence of grain characteristics is not beneficial to constraining the porosity-permeability relationship in these sample suites (Fig. 6). This may be a result of using a Kozeny-Carman fit equation which makes the assumption that grains are spherical producing a simple pore structure (Rahrah et al. 2020). Bear (1972) describes how this assumption arises from the transformation of the specific surface area term (Carman 1937) to a characteristic grain size term.

Inclusion of grain size in the paradigm of a Kozeny-Carman relationship defines the diameter of the grain which is assumed to be spherical. However, we define grain size as the greatest distance from one side of the grain to another or the calliper distance, which is applicable to non-spherical grains. Therefore, as the sphericity of a given grain reduces, it moves further from the Kozeny-Carman assumption which results in a poorer fit to samples with a lower mean grain sphericity. We show that a lower sphericity results in a lower porosity and permeability (Fig. 3) therefore, we would expect the Kozeny-Carman fit to be poorer at lower porosities and permeabilities.

We show it to be the case that lower sphericity or greater grain anisotropy results in a poorer agreement with a Kozeny-Carman based fit (Figs. 5 and 6). It can be observed that below ca. 15% total porosity just one data point lies below the fit line whereas the remaining data points lie consistently and significantly above the fit lines calculated using equation 6. For example, sample PB12 has a low mean grain sphericity of 0.37 and a relatively low total porosity of 9% and can be seen to plot above the black K-C fit line (Fig. 6). This strongly suggests that the Kozeny-Carman style fit is not suitable for use with samples which possess grains which show significantly low sphericities. Torskaya et al. (2014) investigate the effect of grain shape on permeability and find that when using realistic grain shapes from μCT images that the K-C equation underestimates permeability by between 30 and 70%. When using simplified and spherical grain shapes Torskaya et al. (2014) find that the K-C equation fit was far more successful, supporting our conclusion that the K-C spherical grain assumption is causing the poor quality fit. The K-C approach therefore, is not suitable for use with materials where grains are significantly non-spherical.

As a result of this identified limitation, we propose that future work should look to develop an alternative model which accounts for variation in grain sphericity within and between different sandstone samples. In this study we have clearly shown that grain sphericity exhibits a strong relationship with both porosity and permeability (Fig. 3), highlighting the possible value in incorporating this grain characteristic in a porosity-permeability model. A model which is still able to incorporate each influencing factor as individual terms (as in equation 6) would be favourable to provide flexibility and the ability for experimentation. Such a model could be tested against the simple and K-C models presented in Figure 6 based upon RMSE.

Whilst many modified versions of the Kozeny-Carman equation have been proposed and used (e.g., Le Gallo et al. 1998; MacQuarrie and Mayer 2005; Hommel et al. 2018), the fundamental assumption of spherical grains and pores arranged as bundles of capillaries remains. Alternatives to a K-C approach at the same scale have been used to describe permeability such as the Fair-Hatch, Brinkman and Panda and Lake models, described and summarised by Le Gallo et al. (1998) and MacQuarrie & Mayer (2005). Whilst some of these approaches use grain size terms, they do not include terms which allow for direct inclusion of grain shape or anisotropy.

A further consideration which would be highly beneficial to any future model would be to account for the percolation threshold, a key phenomenon which makes effectively characterising the porosity-permeability relationship difficult over a range of porosities. Thomson, et al. (2020b) and Payton et al. (2021) show the percolation threshold for full connectivity to be at ca. 8 - 15% total porosity, whilst Mavko & Nur (1997) and Rahrah et al. (2020) show the value of incorporating the percolation threshold into a K-C style fit. Consideration of the percolation threshold alongside variable grain sphericity would surely be an effective approach to best describe the porosity-permeability relationship.

CONCLUSIONS

In this work we made a comparison of two similar grain segmentation techniques, using marker-based watershed algorithms, for reliable and accurate grain boundary identification across our sample suites. We found that using a median filter in addition to a non-local means (NLM) filter prior to segmentation resulted in superior grain separation as opposed to using a NLM filter alone. This appeared to be due to the ability of the median filter to preserve and enhance the grain edges during denoising, reducing oversegmentation. The low computational cost and high speed at which this technique can be applied makes this a suitable option for segmentation of sandstone materials such as those investigated here.

We have used digital image analysis techniques on μCT images of three different suites of sandstone samples to investigate the impact of grain characteristics on the porosity-permeability relationship. We have shown that in this collection of samples the porosity-permeability relationship is not better constrained when including grain shape and size parameters in a Kozeny-Carman type fit equation. This is the case despite identification of a strong positive relationship between grain sphericity and both porosity and permeability. We found no such relationship with grain size. Therefore, we found a porosity-permeability relationship best described by $K = 10^{5.54}\,\phi^{3.7}$.

We determine that the need to assume that grains are spherical when working in a Kozeny-Carman paradigm is severely limiting to identifying an effective porosity-permeability relationship. Future work should focus on incorporating a grain sphericity term in a model which effectively handles non-spherical and non-uniform grains. Of added benefit would be consideration of the percolation threshold in producing a model capable of constraining the porosity-permeability relationship over a range of porosities in sandstones.

Finally, consideration of grain sphericity as a measure of 3D grain shape anisotropy revealed a relationship of decreasing anisotropy resulting in greater porosity and permeability, in agreement with 2D measures of grain anisotropy. We found total porosity to vary with grain sphericity according to $\phi = 1.22\phi - 0.42$, offering an additional indirect method of predicting porosity. A group of outliers are identified, vertically displaced below the main trend of the sphericity-permeability data. We suggest that this may be due to a lack of grain orientation with regards to sphericity in these samples, inhibiting the permeability only as the same occurrence is not observed so strongly in the case of porosity.

REFERENCE LIST

Barraud J., 2006, The use of watershed segmentation and GIS software for textural analysis of thin sections: Journal of Volcanology and Geothermal Research, v. 154, p. 17–33.

Bear J., 1972, Dynamics of fluids in porous media. American Elsevier.

Berg C.F., 2014, Permeability Description by Characteristic Length, Tortuosity, Constriction and Porosity: Transport In Porous Media, v. 103, p. 381–400.

Beucher S. and Meyer F., 2018, The Morphological Approach to Segmentation: The Watershed Transformation, *in* Mathematical Morphology in Image Processing, 1st edn, CRC Press, p. 433–481.

Blunt M.J., Bijeljic B., Dong H., Gharbi O., Iglauer S., Mostaghimi P., Paluszny A. and Pentland C., 2013, Pore-scale imaging and modelling: Advances In Water Resources: v. 51, p. 197–216.

Buades A., Coll B. and Morel J-M., 2008, Nonlocal Image and Movie Denoising: International Journal of Computer Vision, v.76, p. 123–139.

Buades A., Coll B. and Morel J-M., 2010, Image Denoising Methods. A New Nonlocal Principle: SIAM Review, v. 52, p. 113–147.

Bultreys T., Van Hoorebeke L. and Cnudde V., 2015, Multi-scale, micro-computed tomography-based pore network models to simulate drainage in heterogeneous rocks: Advances In Water Resources, v. 78, p. 36–49.

Campbell A., Murray P., Yakushina E., Marshall, S. and Ion W., 2018, New methods for automatic quantification of microstructural features using digital image processing: Materials and Design, v. 141, p. 395–406.

Carman P.G., 1937, Fluid flow through granular beds: Transaction of the Institution of Chemical Engineers, v.15, p. 150–156.

Cristoforetti A., Faes L., Ravelli F., Centonze M., Del Greco M., Antolini R. and Nollo G., 2008, Isolation of the left atrial surface from cardiac multi-detector CT images based on marker controlled watershed segmentation: Medical Engineering and Physics, v. 30, p. 48–58.

de Lima O.A. and Niwas, S., 2000, Estimation of hydraulic parameters of shaly sandstone aquifers from geoelectrical measurements: Journal of Hydrology, v. 235, p. 12–26.

Fei W., Narsilio G.A. and Disfani M.M., 2019, Impact of three-dimensional sphericity and roundness on heat transfer in granular materials: Powder

Technology, v. 355, p. 770–781.

Fei W. and Narsilio G.A., 2020, Impact of Three-Dimensional Sphericity and Roundness on Coordination Number: Journal of Geotechnical and Geoenvironmental Engineering, v. 146, no. 06020025.

Folk R.L., 1980, Petrology of sedimentary rocks. Hemphill Publishing Company.

Furat O., Wang M., Neumann M., Petrich L., Weber M., Krill C.E. and Schmidt V., 2019, Machine Learning Techniques for the Segmentation of Tomographic Image Data of Functional Materials. Frontiers in Materials, v. 6, no. 145.

Hommel J., Coltman E. and Class H., 2018, Porosity–Permeability Relations for Evolving Pore Space: A Review with a Focus on (Bio-)geochemically Altered Porous Media: Transport In Porous Media, v. 124, p. 589–629.

Huang H., Li X. and Chen C., 2018, Individual Tree Crown Detection and Delineation From Very-High-Resolution UAV Images Based on Bias Field and Marker-Controlled Watershed Segmentation Algorithms: IEEE Journal of Selected Topics in Applied Earth Observations and Remote Sensing, v. 11, p. 2253–2262.

Kong D. and Fonseca J., 2018, Quantification of the morphology of shelly carbonate sands using 3D images: Géotechnique, v. 68, p. 249–261.

Kozeny J., 1927, Über kapillare Leitung des Wassers im Boden: Sitzungsber Akad Wiss Wien, v. 136, p. 271–306.

Le Gallo Y., Bildstein O. and Brosse E., 1998, Coupled reaction-flow modeling of diagenetic changes in reservoir permeability, porosity and mineral compositions: Journal of Hydrology, v. 209, p. 366–388.

Legland D., Arganda-Carreras I. and Andrey P., 2016, MorphoLibJ: integrated library and plugins for mathematical morphology with ImageJ: Bioinformatics, v. 32, p. 3532–3543.

Leonti A., Fonseca J., Valova I., Beemer R., Cannistraro D., Pilskaln C., DeFlorio D. and Kelly G., 2020, Optimized 3D Segmentation Algorithm for Shelly Sand Images: Proceedings of the 6th World Congress on Electrical Engineering and Computer Systems and Science, p. CIST 107.

MacQuarrie K.T.B. and Mayer K.U., 2005, Reactive transport modeling in fractured rock: A state-of-the-science review: Earth-Science Reviews, v. 72, p. 189–227.

Mavko G. and Nur A., 1997, The effect of a percolation threshold in the Kozeny-Carman relation: GEOPHYSICS, v. 62, p. 1480–1482.

Nabawy B.S., 2014, Estimating porosity and permeability using Digital Image Analysis (DIA) technique for highly porous sandstones: Arabian Journal of Geosciences, v. 7, p. 889–898.

Ollion J., Cochennec J., Loll F., Escudé, C. and Boudier T., 2013, TANGO: a generic tool for high-throughput 3D image analysis for studying nuclear organization: Bioinformatics, v. 29, p. 1840–1841.

Otsu N., 1979, A Threshold Selection Method from Gray-Level Histograms: IEEE

Transactions on Systems, Man and Cybernetics, v. 9, p. 62–66.

Payton R.L., Fellgett M., Clark B.L., Chiarella D., Kingdon A. and Hier-Majumder S., 2021, Pore-scale assessment of subsurface carbon storage potential: implications for the UK Geoenergy Observatories project: Petroleum Geoscience, v. 27, no. petgeo2020-092.

Rahrah M., Lopez-Peña L.A., Vermolen F. and Meulenbroek B., 2020, Network-inspired versus Kozeny–Carman based permeability-porosity relations applied to Biot's poroelasticity model: Journal of Mathematics in Industry, v. 10, p. 19.

Schäfer A. and Teyssen T., 1987, Size, shape and orientation of grains in sands and sandstones—image analysis applied to rock thin-sections: Sedimentary Geology, v. 52, p. 251–271.

Schindelin J., Arganda-Carreras I., Frise E., Kaynig V., Longair M., Pietzsch T., Preibisch S., Rueden C., Saalfeld S., Schmid B., Tinevez J-Y., White D.J., Hartenstein V., Eliceiri K., Tomancak P., and Cardona A., 2012, Fiji: an open-source platform for biological-image analysis: Nature Methods, v. 9, p. 676–682.

Shi Y., and Yan W.M., 2015, Segmentation of irregular porous particles of various sizes from X-ray microfocus computer tomography images using a novel adaptive watershed approach: Géotechnique Letters, v. 5, p. 299–305.

Suhr B., Marschnig S. and Six K., 2018, Comparison of two different types of railway ballast in compression and direct shear tests: experimental results and DEM model validation: Granular Matter, v. 20, p.70.

Sun Q., Zheng J. and Li C., 2019, Improved watershed analysis for segmenting contacting particles of coarse granular soils in volumetric images: Powder Technology, v. 356, p. 295–303.

Thomson P-R., Aituar-Zhakupova A. and Hier-Majumder S., 2018, Image Segmentation and Analysis of Pore Network Geometry in Two Natural Sandstones: Frontier in Earth Sciences, v. 6, no. 58.

Thomson P-R., Hazel A. and Hier-Majumder S., 2019, The Influence of Microporous Cements on the Pore Network Geometry of Natural Sedimentary Rocks: Frontiers in Earth Sciences, v. 7, no. 48.

Thomson P-R., Ellis R., Chiarella D. and Hier-Majumder S., 2020a, Microstructural Analysis From X-Ray CT Images of the Brae Formation Sandstone, North Sea: Frontiers in Earth Sciences, v. 8, no. 246.

Thomson P-R., Jefferd M., Clark B.L., Chiarella D., Mitchell T.M. and Hier-Majumder S., 2020b, Pore network analysis of Brae Formation sandstone, North Sea: Marine and Petroleum Geology, v. 122, no. 104614.

Torskaya T., Shabro V., Torres-Verdín C., Salazar-Tio, R. and Revil, A., 2014, Grain Shape Effects on Permeability, Formation Factor, and Capillary Pressure from Pore-Scale Modeling: Transport in Porous Media, v. 102, p. 71–90.

Urumovic K. and Urumovic Sr. K., 2014, The effective porosity and grain size relations in permeability functions: Hydrology and Earth System Sciences Discussions, v. 11, p. 6675–6714.

Veta M., Huisman A., Viergever M.A., van Diest P.J. and Pluim J.P.W., 2011, Marker-controlled watershed segmentation of nuclei in H&E stained breast cancer biopsy images: 2011 IEEE International Symposium on Biomedical Imaging: From Nano to Macro, p. 618–621.

Keller W.D., 1945, Size Distribution of Sand in Some Dunes, Beaches, and Sandstones: AAPG Bulletin, v. 29, p. 215–221.

Wang J-J., Zhang H-P., Deng D-P. and Liu M-W., 2013, Effects of mudstone particle content on compaction behavior and particle crushing of a crushed sandstone–mudstone particle mixture: Engineering Geology, v. 167, p. 1–5.

Wentworth C.K., 1922, A Scale of Grade and Class Terms for Clastic Sediments: Journal of Geology, v. 30, p. 377–392.

Xue Y., Zhao J. and Zhang M., 2021, A Watershed-Segmentation-Based Improved Algorithm for Extracting Cultivated Land Boundaries: Remote Sensing, v. 13, p. 939.

CONFLICT OF INTEREST STATEMENT

The authors declare that the research was conducted in the absence of any commercial or financial relationships that could be construed as a potential conflict of interest.

AUTHOR CONTRIBUTIONS

Conceptualisation: Ryan L. Payton, Domenico Chiarella; Methodology: Ryan L. Payton; Formal analysis and investigation: Ryan L. Payton; Writing - original draft preparation: Ryan L. Payton; Writing - review and editing: Ryan L. Payton, Domenico Chiarella, Andrew Kingdon; Supervision: Domenico Chiarella, Andrew Kingdon.

FUNDING

RLP acknowledges support from a NERC DTP studentship (grant number NE/L002485/1) as well as further financial support through a CASE partnership with the British Geological Survey as part of their British University Funding Initiative.

ACKNOWLEDGEMENTS

The authors would like to thank Paul-Ross Thomson for his useful input regarding the methodology and Frank Lehane (RHUL) for his computational support throughout the project. This manuscript was published with the permission of the Executive Director of the British Geological Survey.

DATA AVAILABILITY STATEMENT

The μCT images used in this article are available from a variety of sources. Images of the Wilmslow Sandstone Fm. for samples with a SF prefix are available from Payton et al. (2021). Images of the Brae Fm. Sandstone for samples with BFS prefix are not publicly available and must be requested from Thomson, et al. (2020b). Images of the Minard Formation Sandstone from the Porcupine Basin for samples with a PB prefix are available from the Royal Holloway, University of London Figshare Repository, https://figshare.com/s/a3c53f2b89fb3d655f6a.

FIGURE CAPTIONS

Figure 1. Schematic diagram showing the typical steps in grain identification using a watershed technique on CT images.

Figure 2. Isolated collection of grains (white) and single grain (orange) shown in 3D from sample SF696. The saw-tooth or staircase pattern is highlighted which arises from the voxelised images. This can lead to overestimation of surface area and impact the subsequent sphericity measurements.

Figure 3. Relationship between mean grain size, mean grain sphericity and total porosity and permeability. A generally positive relationship with porosity and permeability can be observed in the case of mean grain sphericity but no such relationship is present with mean grain size. A region of outliers is identified by a dashed line in **(d)** with the same data points also identified in **(b)**.

Figure 4. Relationship between mean grain sphericity and mean connected pore diameter for each of the three sample suites. It is apparent that there is a generally positive relationship between the two parameters.

Figure 5. Range of calculated fit configurations to the porosity-permeability relationship which incorporate grain characteristics using a Kozeny-Carman based relationship. The table to the right qualitatively describes the difference between each fit line whilst the respective equations are displayed in the plot legend.

Figure 6. Calculated fits to the porosity-permeability relationship. The root mean square error (RMSE) values are reported for each fit, showing that the better fit is the simpler one in green. The green fit excludes any measured grain characteristics whereas the black fit does not.

Figure 7. Comparison of two different filtering techniques' effect on the watershed algorithm in a single slice of sample PB10. Four different locations have been highlighted for comparison on an image which has undergone non-local means (NLM) filtering only. Annotated squares show the result of watershed grain segmentation following only NLM (Thomson et al. 2020a) and NLM with a median filter (Fei and Narsilio 2020). Each grain can be identified by a different colour however, due to the number of grains, colours have been

reused and instead the black grain boundaries split different grains of the same colour. In each annotation an example of over-segmentation is observed in the case of using NLM filtering only when compared to what we might expect from the CT image. The outer scale bar applies to all annotations.

Table 1. Summary of the sampled materials analysed in this study.

*Payton et al. (2021), **Thomson et al. (2020b).

Sampling Location	Well ID	Sample ID	Depth (m)	Geology	
Porcupine Basin, N. Atlantic	26/28-1	PB01 PB02 PB03 PB05	2271 2256.4 2420 2420.48	Minard Formation	Renard Member Dooneragh Member
	26/28-2	PB06 PB07 PB08 PB10 PB11 PB12	2117 2118 2116.8 2118.6 2119.15 2119.85		
Sellafield, UK*	SFBH13B	SF696 SF697 SF698 SF699 SF700 SF701 SF702	63.8 76.1 96.98 126.27 144.03 172.16 181.39	Wilmslow Sandstone Formation	
North Sea, UK**	16/7b-20	BFS1 BFS2 BFS4	4040.1 4041.35 4045.13	Brae Formation Sandstone	
	16/7b-23	BFS5 BFS8	4061 4063.75		

Table 2. Grain-based measurements made for each sample.

Sample	Sorting (ϕ)	Mean Grain Size (μm)	Mean Grain Sphericity

PB01	0.63	242	0.45
PB02	0.61	298	0.43
PB03	0.44	112	0.47
PB05	0.45	297	0.47
PB06	0.55	198	0.46
PB07	0.45	92	0.44
PB08	0.42	168	0.48
PB10	0.49	120	0.45
PB11	0.78	223	0.40
PB12	0.56	117	0.37
SF696*	0.61	203	0.49
SF697*	0.54	205	0.46
SF698*	0.64	204	0.52
SF699*	0.50	257	0.53
SF700*	0.51	230	0.46
SF701*	0.51	179	0.50
SF702*	0.52	247	0.45
BFS1**	0.61	135	0.44
BFS2**	0.75	262	0.43
BFS4**	0.69	158	0.44
BFS5**	0.53	421	0.43
BFS8**	0.44	108	0.46

*Payton et al. (2021), **Thomson et al. (2020b).

Table 3. Porosity and permeability measurements made for each sample.

Sample	Total Porosity (%)	Connected Porosity (%)	Permeability (mD)
PB01	20.4	20.3	1070
PB02	10.5	9.8	147
PB03	12.2	10.2	99
PB05	11.2	4.9	37
PB06	6.7	5.2	21
PB07	9.6	8.9	46
PB08	13.6	13.3	123
PB10	12.9	9.7	237
PB11	14.1	13.6	36
PB12	9	6.9	18
SF696[*]	20.7	20.4	1760
SF697[*]	20.7	20.3	620
SF698[*]	22.9	22.7	3190
SF699[*]	26.4	26.3	6040
SF700[*]	17.0	16.6	360
SF701[*]	24.3	24.1	1420
SF702[*]	9.77	8.89	40
BFS1[**]	7.2	5.8	91
BFS2[**]	7.1	5.7	86
BFS4[**]	9.6	9.1	104
BFS5[**]	7.8	5.1	6.7
BFS8[**]	15.2	14.8	795

[*]Payton et al. (2021), [**]Thomson et al. (2020b).